Brownian motion of tethered nanowires

Sadao Ota,[1,2] Tongcang Li,[1,3] Yimin Li,[1] Ziliang Ye,[1] Anna Labno,[1] Xiaobo Yin,[1,3]
Mohammad-Reza Alam,[2] and Xiang Zhang[1,2,3,*]

[1]*NSF Nano-scale Science and Engineering Center (NSEC), 3112 Etcheverry Hall, University of California, Berkeley, California 94720, USA*
[2]*Department of Mechanical Engineering, University of California, Berkeley, California 94720, USA*
[3]*Material Sciences Division, Lawrence Berkeley National Laboratory, 1 Cyclotron Road, Berkeley, California 94720, USA*

(Received 1 August 2013; revised manuscript received 28 January 2014; published 13 May 2014)

Brownian motion of slender particles near a boundary is ubiquitous in biological systems and in nanomaterial assembly, but the complex hydrodynamic interaction in those systems is still poorly understood. Here, we report experimental and computational studies of the Brownian motion of silicon nanowires tethered on a substrate. An optical interference method enabled direct observation of microscopic rotations of the slender bodies in three dimensions with high angular and temporal resolutions. This quantitative observation revealed anisotropic and angle-dependent hydrodynamic wall effects: rotational diffusivity in inclined and azimuth directions follows different power laws as a function of the length, $\sim L^{-2.5}$ and $\sim L^{-3}$, respectively, and is more hindered for smaller inclined angles. In parallel, we developed an implicit simulation technique that takes the complex wire-wall hydrodynamic interactions into account efficiently, the result of which agreed well with the experimentally observed angle-dependent diffusion. The demonstrated techniques provide a platform for studying the microrheology of soft condensed matters, such as colloidal and biological systems near interfaces, and exploring the optimal self-assembly conditions of nanostructures.

DOI: 10.1103/PhysRevE.89.053010 PACS number(s): 47.60.−i, 83.85.Ei, 68.08.−p, 82.70.Dd

I. INTRODUCTION

Microscopic slender objects such as bacterial and sperm cells [1–4], flagella [5], microtubules [6], nanotubes [7,8], and nanowires [9–11] suspended in a liquid are subject to Brownian fluctuation due to random collision of the liquid molecules. The mean-square displacement of Brownian motion is proportional to the inverse of the frictional coefficients that count the viscous drags from surrounding fluid flows. This is described in the Einstein relation of diffusivity, $D = k_B T/\eta\Gamma$, where k_B is the Boltzmann constant, T is temperature, η is fluid viscosity, and Γ is the hydrodynamic friction tensor. Near a surface, the flows induced by the Brownian motion of the particle are reflectively modified and in turn affect the particle's motion, and such hydrodynamic interaction (HI) generally causes anisotropic increase of the components of the friction tensor Γ. This complex anisotropic friction tensor leads to anisotropic Brownian motion. In most realistic situations in technological or biological systems [1–18], microscopic objects are confined by boundaries such as substrate surfaces and cell membranes. Understanding their HI with a nearby boundary is crucial for understanding the real dynamics in the motion of molecules and cells [1–7,17–19], as well as the self-assembly of colloidal objects [8–11,13–15]. Unlike the sphere-wall HI that has been well studied extensively [20–24], however, much more complex HIs between slender particles and a wall are still poorly understood. Especially, little is known about the diffusive behavior of objects in contact with the wall [23,24].

The Brownian motion of the slender particle is subject not only to the solvent flows reflected from the environment, but also to those induced by the motion of itself [12,13,14,16,19]. Recent studies have advanced our understanding of the effect of such HI induced by the particle itself in an isotropic environment, such as the coupling between the translational and the rotational diffusions of rodlike particles [12,14,16]. However, the HI with the nearby interfaces further increases the complexity and has hampered its theoretical understanding [13,14]. Experimentally, it is difficult to observe the near-wall Brownian motion of the slender particle with conventional optical methods because of complicated light scatterings. Particularly, a direct visualization of the minute change of the inclined angle between the moving particle and the surface has been elusive [14,17] and previous works typically assumed the particle being parallel to the wall [12,25]. In this work, we report an experimental study of the Brownian motion of nanowires *tethered* on a substrate. We developed a dynamic interference imaging technique to visualize the three-dimensional (3D) diffusive motion of tethered nanowires *in situ* and, together with our hydrodynamic model, directly observed their complex HI near the surface.

II. INTERFEROMETRIC IMAGING METHOD

In our experiment, a suspension of silicon nanowires (150 nm in diameter, with lengths varying from 5 to 25 μm) was stored in a closed chamber on a glass cover slip. Some of the nanowires had one end tethered to the glass surface due to the van der Waals force [Fig. 1(a)] and the other end free, undergoing Brownian rotation around the tethered point. The nanowires used in the experiments are rigid enough such that bending is negligible (Appendix A). The electrostatic force was negligible in our experiment since the solution was at relatively high ion strength (10 mM of KCl). When monochromatically illuminated, the light backscattered from the nanowire interferes with the light reflected from the glass-water interface, producing a modulated pattern along the wire. This interference pattern can be used to measure the inclination

*Corresponding author: xiang@berkeley.edu; Present address: 3112 Etcheverry Hall, University of California, Berkeley, CA 94720, USA.

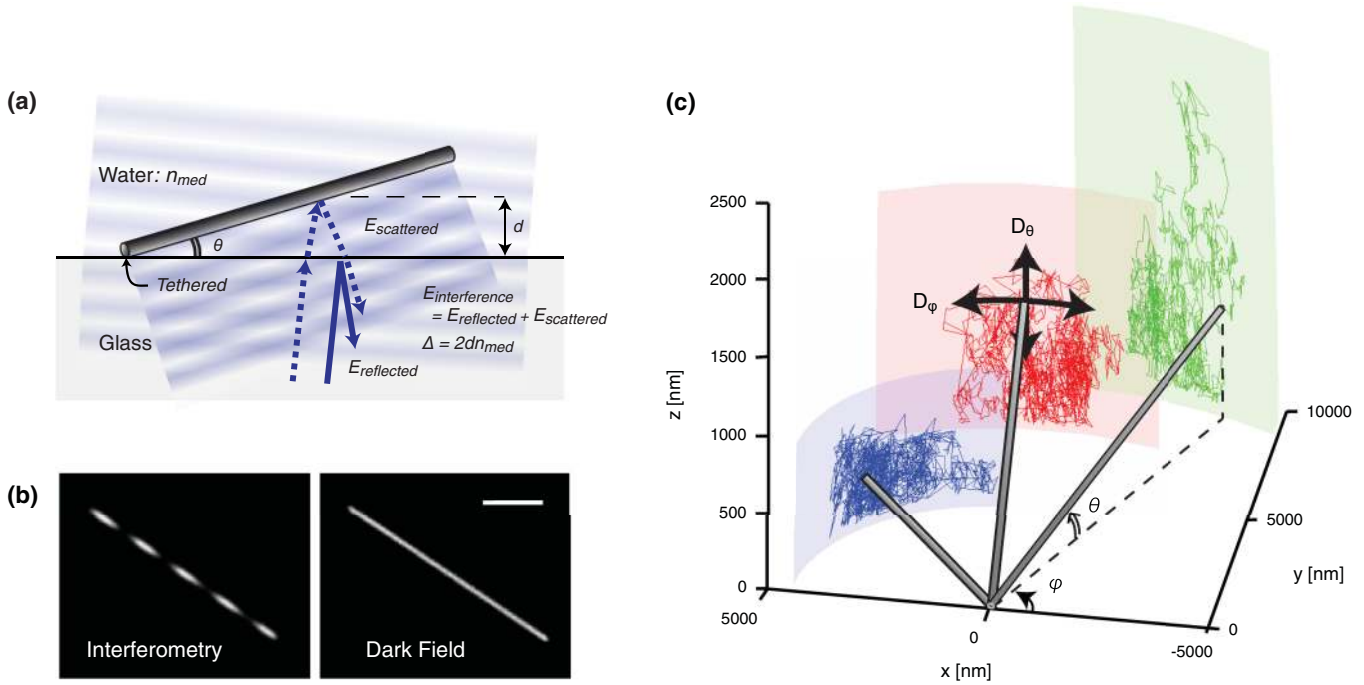

FIG. 1. (Color online) Backscattering interference contrast microscopy (BICM) for characterizing dynamic Brownian motion of nanowires tethered to a wall. (a) Schematic diagram of the BICM. One end of a uniform silicon nanowire (150 nm in diameter) in water is tethered to a glass surface while the other end freely diffuses. A monochromatic light is applied to the sample with a small illumination angle. The backscattered light from the nanowire interferes with that reflected from the water-glass interface, producing a periodic interference pattern along the wire. (b) An interference image (left) and a dark-field image (right, scale bar = 5 μm) of the same nanowire taken using the same objective. A single interference image allows us to measure both inclined (θ) and azimuth (ϕ) angles of the tethered nanowire at once with high spatial and temporal resolutions. (c) A sequence of interference images enables tracking the Brownian motion of the tethered nanowire, revealing the complex hydrodynamic interactions (HIs) between the wires and a wall.

angle (θ) at high angular (up to $\sim 10^{-5}$ rad, corresponding to 1 Å displacement of the free end of a 10-μm nanowire) and temporal (<0.004 s) resolutions, while a dark-field image cannot [Fig. 1(b); also see Appendix A and Supplemental Material [26]). Direct measurement of the azimuth angle (φ) at a high resolution (up to an order of $\sim 10^{-5}$ rad) was achieved by fitting the image of the nanowire with a single ellipse. A single interference image thus measures both the inclined and the azimuth angles simultaneously, allowing us to track the 3D Brownian motion of the tethered nanowires accurately [Fig. 1(c)]. In general, nanoscopic objects were not suitable for reflection interference contrast microscopy [27] because they only weakly scatter light and induce significant phase shifts. Here we utilize the fact that the silicon nanowires strongly scatter visible light due to Mie resonance [28] and the interference period is not affected by the phase shifts. The latter is because the diameter of each high-quality nanowire is uniform along its length, so the phase shift occurs uniformly along each wire (Appendix A).

The continuous measurement of the 3D Brownian motion of tethered nanowires clearly revealed the length-dependent anisotropic reduction in their rotational diffusion, attributed to the complex HI. Figure 2(a) displays typical angular mean-square displacements of nanowires over time: AMSD = $\langle \Delta\theta^2, \Delta\phi^2 \rangle$. It was observed that both $\langle \Delta\theta^2 \rangle$ and $\langle \Delta\phi^2 \rangle$ of all nanowires increase linearly at short time scales (<0.1 s), so their motions were diffusive and followed the general law of Brownian motion: AMSD = $\langle \Delta\theta^2, \Delta\phi^2 \rangle = 2D_{\theta,\phi}\Delta t$. From the slopes, we obtained the angular diffusivities ($D_{\theta,\varphi}$) for the nanowires with lengths ranging from 5 to 25 μm. At longer time scales, the mean-square displacement reached a plateau with large fluctuations. This was likely due to a combination of multiple factors including the geometric restriction from the wall and the restoring forces from the wire-wall joints, and the gravity [29]. In Fig. 2(b), compared to the analytically calculated free rotational diffusivity of a nanowire, the measured rotational diffusivities clearly show the hindered, anisotropic diffusion due to the HI with the wall. The reduction in D_θ was larger than that in D_ϕ because a larger portion of reflected flows from the wall is directed back toward the wire, which preferentially reduced the diffusion in the θ direction. The D_θ and D_ϕ clearly follow different power laws as a function of the length, $\sim L^{-2.5}$ and $\sim L^{-3}$, in good approximation for the rods we observed (<6% and <3% errors, respectively). These power laws resulted in more significant anisotropy in the rotational motion for shorter nanowires since $D_\phi/D_\theta \sim L^{-0.5}$. These indicate that a shorter wire experienced more significant HI as it has a larger portion of its length near the surface.

While Fig. 2 shows the overall diffusive behavior of the tethered nanowires, our fast and accurate technique further enabled measurement of angle-dependent HIs that dynamically change

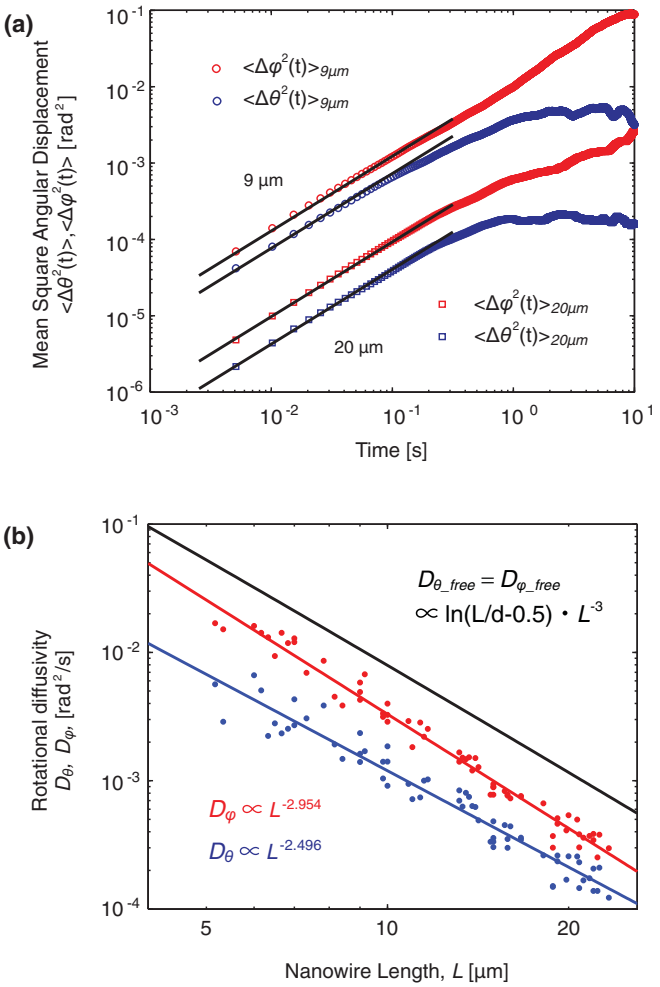

FIG. 2. (Color online) Measurement of overall angular mean-square displacements (AMSD $= \langle \Delta\theta^2, \Delta\phi^2 \rangle$) of the tethered nanowires and their rotational diffusivities. (a) A double logarithmic plot of the overall $\langle \Delta\theta^2 \rangle$ and $\langle \Delta\phi^2 \rangle$ of sample nanowires shows the diffusive behavior ($\propto t$, shown as black lines with slope 1) at short time scales (<0.1 s). Blue and red circles are the inclined and azimuth $\langle \Delta\theta^2 \rangle$ and $\langle \Delta\phi^2 \rangle$ of a 9-μm nanowire. Squares are those of a 20-μm nanowire. Their position data were taken at 250 and 180 Hz, respectively, for more than 30 000 frames. (b) The rotational diffusivities of the tethered nanowires in the inclined (D_θ, red circles) and azimuth (D_ϕ, blue circles) orientations show more significant hydrodynamic wall effect in D_θ in an anisotropic manner. The black curve is an analytical solution for free rotational diffusivity of a cylindrical rod (no wall). D_θ and D_ϕ clearly follow different power laws as a function of the length, $\sim L^{-2.5}$ and $\sim L^{-3}$, in good approximation for the rods we observed (<6% and <3% errors, respectively). These power laws resulted in more significant anisotropy in the rotational motion for shorter nanowires as $D_\phi / D_\theta \sim L^{-0.5}$. The data were taken from 65 wires in total.

during the long time diffusion. The overall trajectories used in Fig. 2 were sorted according to the initial inclined angle, θ_{init}, and the values of $\langle \Delta\theta^2 \rangle$ and $\langle \Delta\phi^2 \rangle$ were recalculated for each sorted subset. At short time scales, the $\langle \Delta\theta^2 \rangle$ and $\langle \Delta\phi^2 \rangle$ sorted for different θ_{init} increased linearly with different slopes.

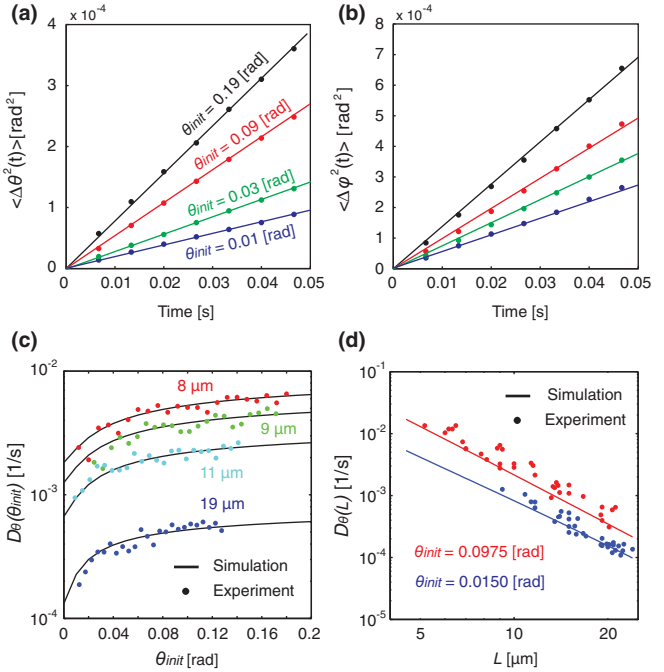

FIG. 3. (Color online) Measured and calculated diffusion dependence on inclined angle and wire length. Representative plots of sorted $\langle \Delta\theta^2 \rangle$ and $\langle \Delta\phi^2 \rangle$ in the inclined (a) and the azimuth (b) shows the diffusive behavior at short time scale (<0.05 s), but at different slopes (diffusivity) depending on the initial inclined angle θ_{init}. The sample data were of 9-μm nanowire and sorted with θ_{init} by every 0.02 rad. From top to bottom, the initial inclined angles are 0.19 (black), 0.09 (red), 0.03 (green), and 0.01 (blue) rad. (c), (d) are the inclined angle- and/or length-dependent rotational diffusivities of the tethered nanowires, D_θ, obtained from the slopes in (a), (b). The results clearly show significant hydrodynamic wall effects when the wires are closer to the wall. (c) Comparison between the measured angle-dependent rotational diffusivities (dots) and the numerically calculated ones (curves) at four different wire lengths. (d) Comparison between the measured length-dependent rotational diffusivities for a large number of sample wires (dots) and the numerically calculated ones (curves) at two different θ_{init}. Both (c) and (d) show experimentally measured diffusivity quantitatively agrees well with calculated values without any fitting parameters.

The slope apparently dropped as the θ_{init} decreased [Figs. 3(a) and 3(b)]. The angle-dependent diffusivity was then evaluated as the half slope of each sorted $\langle \Delta\theta^2 \rangle$: $D_\theta(L, \theta_{\text{init}}) = \frac{\langle \Delta\theta^2 \rangle}{2\Delta t}$. It was approximately independent of Δt at sufficiently short time scales (<0.05 s; see Appendix A), suggesting that it followed typical Brownian motion with this locally determined diffusivity. At long time scales, the nanowires move from θ_{init} to different positions, where they experience different HIs and other confinement effects from environments, resulting in a deviation from the original local D_θ. The final results in Figs. 3(c) and 3(d) show the increasingly more significant reduction in local D_θ as the initial inclined angle θ_{init} becomes smaller. Here we focused on the diffusive rotation into the inclined orientation, where the more significant wall effect was observed. In Figs. 3(c) and 3(d), the experimental results (dots) and the simulated ones (curves) were plotted together and show

excellent agreement with no fitting parameter, demonstrating the dominance of the hydrodynamic forces in the system and the powerfulness of our experimental and numerical approaches.

III. IMPLICIT THREE-DIMENSIONAL HYDRODYNAMIC SIMULATION

To fully understand the effect of hydrodynamic interactions in the system, we developed a 3D hydrodynamic model based on a string-of-beads idealization of the system, and implicitly solved it for the hydrodynamic velocity of each bead [19]. Here we introduce the basic idea of the model with Fig. 4(a), in which we consider two beads B_1 and B_2 located at $\vec{X}_1$ and $\vec{X}_2$, respectively, as the simplest case (generalized in Appendix B). If B_1 moves with a steady speed $\vec{v}_1$ (while B_2 is stationary) in the Stokes regime, a steady speed $\vec{v}_{1H,2}$ will be induced at the location $\vec{X}_2$. B_1's motion thereby exerts a drag proportional to the induced velocity $\vec{v}_{1H,2}$ on the bead B_2 and consequently causes its drift. If the bead B_2 also moves with a translational velocity $\vec{v}_2$, the hydrodynamic velocities of each bead, i.e., velocity of each bead relative to the velocity of its surrounding fluid, are given by the following implicit formula [7]:

$$\vec{v}_{1H} = \vec{v}_1 - \vec{v}_{2H,1}, \tag{1}$$

$$\vec{v}_{2H} = \vec{v}_2 - \vec{v}_{1H,2}. \tag{2}$$

Generalization of Eqs. (1) and (2) to N beads leads to

$$\vec{v}_{iH} + \sum_{j=1, j\neq i}^{N} \vec{v}_{jH,i} = \vec{v}_i. \tag{3}$$

Therefore the problem of hydrodynamic velocities of a system of N beads reduces to a system of linear algebraic equations that can be solved using standard methods. The input absolute velocities, $\vec{v}_i$, are given to individual beads assembling the wire and wall, and constrain their shape fixed with respect to each other. For example, when a wire rotates at the angular velocity $\vec{\omega}$ and the nth bead composing the wire has distance $|\vec{r}_n|$ from the tether, the absolute rotational velocity of $|\vec{r}_n|\vec{\omega}$ is given to the bead as input. After obtaining the hydrodynamic velocity of each bead, one can calculate the rotational friction coefficient $\xi_{\rm rot}$, which reflects the complex hydrodynamic interaction with the wall. Since the translational friction coefficient for the spherical bead with diameter d in media having viscosity μ_w is $\xi_0 = 3\pi d\mu_w$, the torque equation is

$$\xi_{\rm rot}\omega_0 = \sum_{k=\text{beads}} |\vec{r}_k \times \xi_0 \vec{v}_{kH}|, \tag{4}$$

where $\vec{r}_k$ is the position vector of the bead B_k from the tethering point. Finally, the rotational diffusivity is proportional to the inverse of the rotational friction coefficient: $D_{\rm rot} = k_B T/\xi_{\rm rot}$. In performing numerical simulations, the extent of the bottom wall was increased until computational results were asymptotically converged (Appendix B).

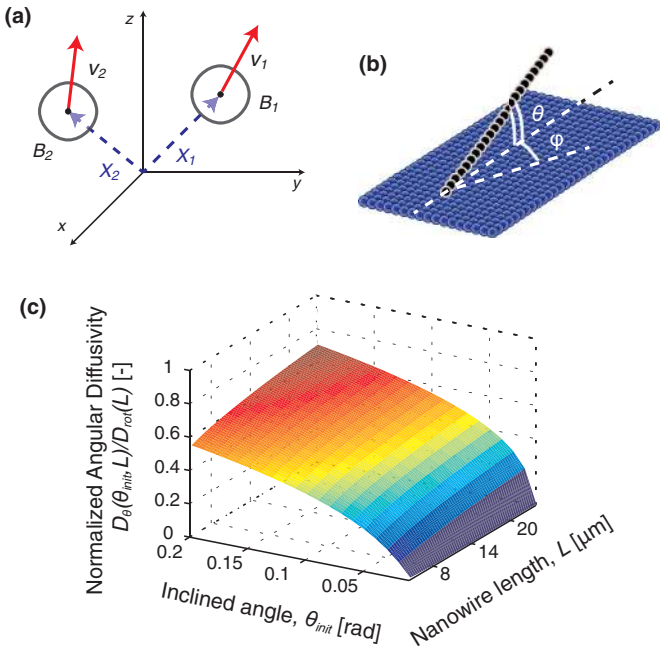

FIG. 4. (Color online) The 3D implicit hydrodynamic simulation of the nanowire diffusion near a wall. (a) The implicit solution for the hydrodynamic velocity, the velocity of each bead relative to its surrounding fluid, considers Stokes superposition of solvent flows efficiently (moving two beads are examples that cause multi-reflected complex flows between them as described in Appendix B). The model enables simulation of very large systems including the complex HI between the wire and a wall. (b) The schematics of the numerical models, wherein the wire and the wall are expressed as a chain and a 2D array of beads, respectively. (c) The inclined angular diffusivity of the tethered wire with different lengths and with different inclined angles, $D_\theta\,(\theta_{\rm init}, L)$, was comprehensively calculated in the developed 3D beads model [normalized by the rotational diffusivity calculated for a free nanowire around its one end, $D_{\rm rot}\,(L)$]. The simulation result shows significant hydrodynamic wall effects when the wires are shorter and/or closer to the wall, which quantitatively agrees well with the experimental observations.

Our approach simplifies the numerical calculation by considering only the Stokes drag between the composing individual beads, which is justified since the solution of the relative velocity includes the effect of multireflected Stokes flow. The model is far more efficient than the molecular dynamic simulation that is incapable of modeling such large systems. We first simulated the free rotational angular diffusivity of a thin rod around its center as a chain of beads in two-dimensional (2D) space. The results agreed well with an analytical approximation (Appendix B). We then extended the model to 3D space for studying the hydrodynamic wall effects by modeling the wall as a 2D array of beads and the tethered wire as a chain of beads [Fig. 4(b) and Appendix B]. Since the nanowire experienced different θ during the long time diffusion, we performed comprehensive calculation of D_θ for a wide range of wire lengths and $\theta_{\rm init}$. The free rotational diffusivity of the tethered wire around its end, $D_{\rm rot}$, was also calculated for normalization. From the calculated hydrodynamic wall effects visualized in Fig. 4(c), we see the HI become increasingly significant as the wire lengths

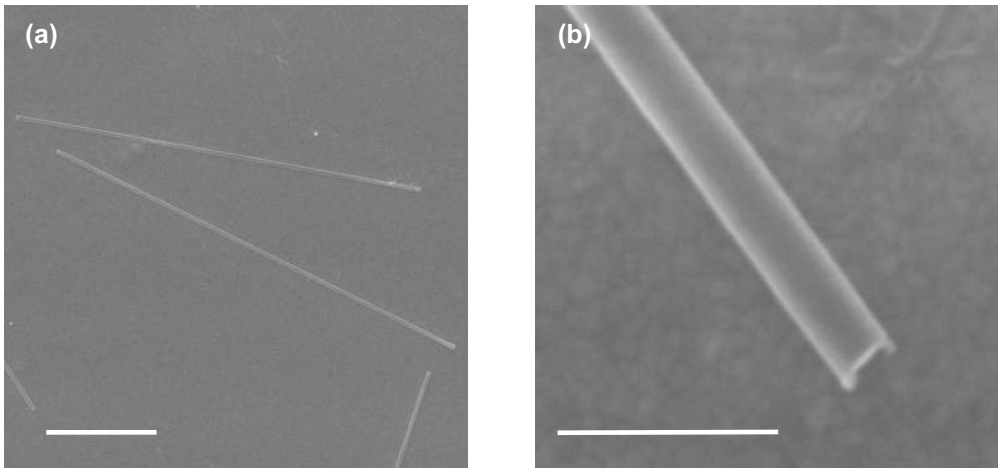

FIG. 5. High-quality rigid silicon nanowires. (a) A scanning electron microscope (SEM) image of highly uniform silicon nanowires with 150-nm diameter (from Sigma, scale bar = 5 μm). (b) A magnified SEM image of an end of the nanowire (scale bar = 500 nm).

and/or the θ_{init} decrease, which quantitatively agreed with our experimental observations.

For comprehensive analysis of the HI, we also calculated the D_φ with several sets of the wire lengths and θ_{init}. As expected from the results in Fig. 2(b), the effects of HI on D_φ were much smaller than that on D_θ. As a result, the anisotropy in the hydrodynamic effect becomes quite significant when θ_{init} become close to zero (see Appendix B and [26]). It may contribute to the efficient functioning of diffusive motor proteins [18,30,31] such as kinesin and F_1F_0-ATPase beside walls. In general, the observed HI also affects the near-interface diffusion of anisotropic biological objects [1–6,17–19] including the cells and filamentous macromolecules. Extending our numerical approach to study the 3D motion of semiflexible objects is straightforward [19] and we thus believe that it can also simulate the near-interface HI in these biophysical systems.

IV. CONCLUSION

In summary, we have studied the Brownian motion of tethered nanowires with high spatiotemporal resolutions, offering fundamental insights for understanding the near-wall diffusion of slender particles. Our interferometry technique together with the versatile calculation method provides powerful platforms for studying interfacial microrheology of various soft condensed matters including the biological particles near cellular and artificial membranes [18,30–32]. For the nanomaterial self-assembly on a substrate, the quantitatively validated string-of-beads model is an efficient tool for optimizing the conditions, which potentially reduces the position inaccuracy caused by the thermal fluctuation and hydrodynamic forces [8–11]. In the near future, use of ferromagnetic nanowires will enable active interfacial microrheology and further explore the rich dynamical response of fluids near surfaces [33–35].

ACKNOWLEDGMENT

The authors acknowledge funding support by the National Science Foundation (NSF) Materials World Network (Grant No. DMR-1210170).

APPENDIX A: EXPERIMENT

Our interference contrast microscopy requires a high-quality scattering surface that is uniformly smooth and flat along the length of the wire. The commercialized silicon nanowire satisfies this uniformity both in diameter and in flatness [Fig. 5(a)]. The magnified image in Fig. 5(b) shows that the wire end is neither perfectly spherical nor flat. It is likely that this roughness could contribute to constrain the rotational diffusion of tethered wires, which appeared as plateaus in the long time scales of the observation in Fig. 2(a). The nanowires used in the experiments are rigid enough such that bending is negligible. For the nanowires in liquid, the possible effect of bending on Brownian motion can be characterized by the persistence length, $L_{\text{p}} = \kappa/k_{\text{B}}T$, where κ is the bending stiffness. $\kappa = EI$, where E is the elastic modulus and I is the area moment of inertia about the filament axis ($I = \pi d^4/64$). Using the Young's modulus of silicon ($E \sim 130$ GPa) and assuming that the silicon nanowires are cylinders with diameter $d = 150$ nm, we obtain the persistent length to be $L_{\text{p}} = 785$ m, which is far longer than the length of the nanowire we used (<20 microns).

Figure 6 depicts the experiment setup of the backscattering interference contrast microscopy (BICM). A mercury lamp was used as the light source, from which monochromatic light was selected using band-path filters. The monochromatic light passed through a narrow aperture of 0.5 mm placed at the Fourier plane and was focused onto the glass surface plane with an objective lens [Carl Zeiss, 50× LD Epiplan HD DIC, working distance (WD) = 6.5 mm, numerical aperture (NA) = 0.5]. The same lens then collected the backscattered light from the nanowire together with the reflected light from the glass-water interface, generating the interference pattern along

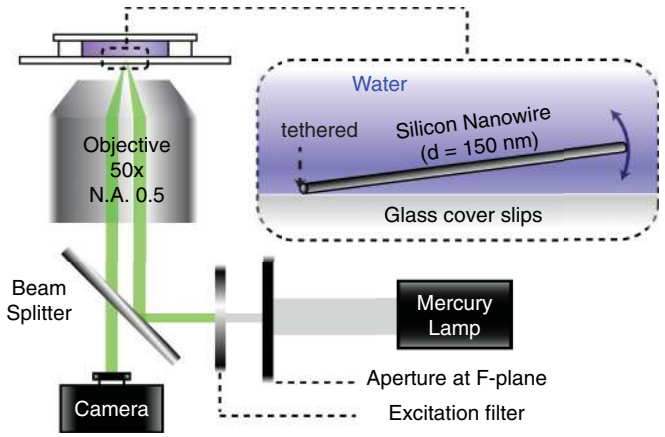

FIG. 6. (Color online) Experimental setup of backscattering interference contrast microscopy (BICM).

the wire. We interpreted the intensity profile of the interference pattern, I, to calculate the inclination angle according to Eq. (A1),

$$2I = (I_{\max} + I_{\min}) - C\frac{I_{\max} - I_{\min}}{2} \times \cos\left\{\frac{4\pi n_w}{\lambda}\left[h - \sin^2\left(\frac{\alpha}{2}\right)\right] + \Phi\right\}, \quad \text{(A1)}$$

where $I_{\max}$ and $I_{\min}$ are maxima and minima intensity of the interference pattern, C is correction constant in contrast amplitude, n_w is refractive index of water, h is the distance from the wall, α is half the illumination cone angle defined with illumination numerical aperture as INA $= n_w \sin\alpha$, and Φ is the phase shifts seen in the pattern. As the nonzero numerical aperture introduces effects of damping the interference contrast and of slightly stretching its periods, represented as C and α, we placed the small aperture of 0.5 mm diameter at the Fourier plane and effectively reduced the INA to 0.05 for minimizing the measurement errors.

While we note that reflection interference contrast microscopy has been used to track microscale objects, its application for nanoscale objects including nanowires is limited. This is because those subdiffractive objects can scatter light with significant phase shift and the signals become weaker. We instead utilized the fact that the silicon nanowire generates strong scattering signals owing to its Mie resonance under visible light illumination and its intrinsically high optical index ($n \approx 4$). Furthermore, as the phase shift Φ uniformly appeared along their highly flat 1D surfaces, the scattered light stayed in a phase and the interference period was thus maintained, enabling our BICM.

As shown in Fig. 7 we calibrated and confirmed the accuracy of the BICM. We partially deposited silicon dioxide layer with e-beam evaporation and, after enclosing the SiO_2 structure in the chamber, introduced the nanowire solution

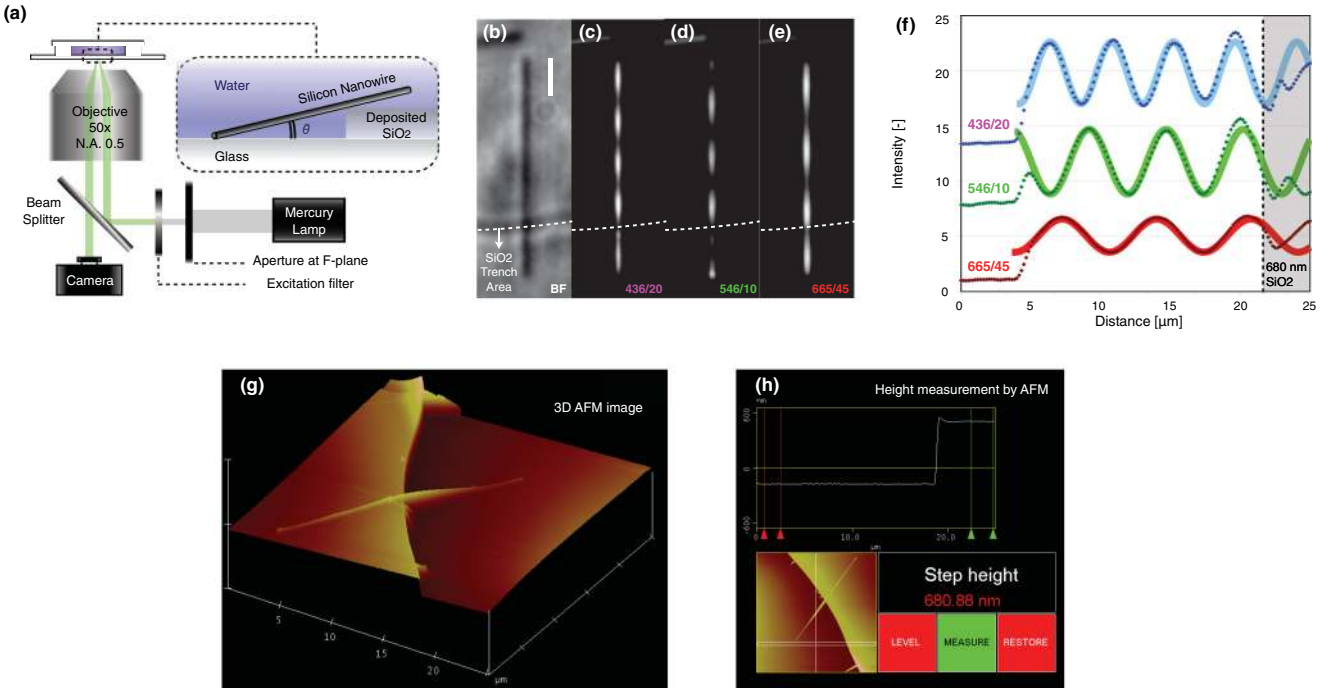

FIG. 7. (Color online) Calibration of the BICM using nanowires on fabricated structures. (a) A partially deposited silicon dioxide layer was used to have the wires leaning and immobilized on the fabricated structured at a fixed inclined angle. (b) Transmission bright-field image of the leaning wire, where its upper area above the dashed line is the surface of the original cover slip and the lower area is the surface of the deposited structure. (c) Backscattering interference contrast image under illumination of light at wavelength of 436 ± 10 nm, (d) is at 546 ± 5 nm, and (e) is at 665 ± 22 nm. In (f), plots show the intensity profile measured along the wire length in the image (b)–(d), while the curves are drawn according to Eq. (1) for each color. The heights of the SiO_2 structure measured by BICM were 673.98 nm at $\lambda = 436 \pm 10$ nm, 675.8 nm at $\lambda = 546 \pm 5$ nm, and 672.17 nm at $\lambda = 665 \pm 22$ nm. After the BICM measurement, we dried the chamber and measured the geometry of the structures with AFM as 681 nm (g) and (h).

at high ion strength. After waiting for a long enough time, some nanowires settled down at the bottom and leaned on the edge of the deposited SiO_2 structure [Fig. 7(a)]. We applied BICM for the leaning nanowire that did not diffuse any more. We performed the measurement on nanowires kept in water because, when they dried, the nanowire would be bent due to capillary forces as seen in Fig. 7(g). We used the same mercury lamp and the objective lens. Figure 7(b) is the transmission bright field image of the wire leaning on the SiO_2 structure. The upper area above the dashed line is the surface of the original cover slip and the lower area is the surface of the deposited SiO_2 structure. Figure 7(c) is the backscattering interference contrast image under illumination of light at a wavelength of 436 ± 10 nm, Fig. 7(d) is at 546 ± 5 nm, and Fig. 7(e) is at 665 ± 22 nm. In Fig. 7(f), plots show the intensity profile measured along the wire length in the image, Figs. 7(b)–7(d), while the curves are drawn according to Eq. (1) with $\lambda =$ 436, 546, and 665 nm. For the wavelength of 546 nm, we can clearly see the significant shift in phase caused by the resonance of the nanowire. The diameter of the nanowire is comparable to the effective wavelength of visible light at the refractive index of silicon, and thus the nanowires were at Mie resonance when applied to visible light. Since this phase shift does not affect the periodicity of the interference pattern, the theoretical curve could be fit well with the measured intensity profile. For the fitting, Φ for 436 and 665 nm were zero while Φ for 546 nm was 0.4. The heights of the SiO_2 structure measured by BICM were 673.98 nm at $\lambda = 436 \pm 10$ nm, 675.8 nm at $\lambda = 546 \pm 5$ nm, and 672.17 nm at $\lambda = 665 \pm 22$ nm. The fitting was made from left side of the interference pattern since its right side near the deposited SiO_2 structure was distorted due to the complex light scattering by the edge of the deposited wall. After the BICM measurement, we dried the chamber and measured the geometry of the structures with AFM [Figs. 7(g) and 7(h)]. The strong surface tension generated in drying the structures distorted the nanowire towards the bottom, as seen in Fig. 7(g). The measured step height of the deposited structure was 681 nm [Fig. 7(h)]. With consideration of the layers of dried solutes, we confirmed the accuracy of our optical measurement.

In the experiment of tracking the Brownian motion of the tethered nanowires, the original solution of highly uniform silicon nanowires (150 nm in diameter and 20 μm in length) in isopropanol was purchased from Sigma-Aldrich. We replaced the isopropanol of the original solution with de-ionized water, by repeated centrifugation. For preparing wires with different lengths, we intensely sonicated the solution to randomly break the long nanowires into short ones. Finally, immediately after increasing the ionic strength, the solution was infused to a premade chamber described below. A clean cover slip was prepared by RCA cleaning with a 1:1:5 solution of NH_4OH, H_2O_2, and H_2O, followed by rigorous washing in de-ionized water and drying with nitrogen blow. An adhesive separator with 0.15 mm height (Sigma-Aldrich) was placed on the cover slip to form a chamber and was sealed with an adhesive sealing tape (Sigma) after introducing the nanowire solution. The chamber was stable enough for observing the Brownian motion of particles for several weeks after sealing. A normal inverted optical microscope from Zeiss was used for all observations. The incoherent light from a mercury lamp was reflected by a

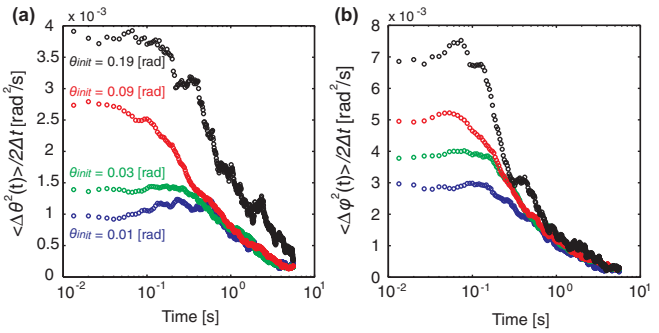

FIG. 8. (Color online) (a), (b) Estimation of the local rotational diffusivity of the nanowire. Local rotational diffusivities in azimuth and inclination directions, respectively, calculated from the linear slopes in Figs. 3(a) and 3(b) (in the main text) with the general law of random diffusion, $\langle \Delta\theta^2 \rangle = 2D_\theta \Delta t$. From bottom to top, blue plots are 0.01 rad at $t = 0$, green are 0.03, red are 0.09, and black are 0.19. Each color corresponds to that plot in Figs. 3(a) and 3(b) in the main text.

50:50 beam splitter and applied to the sample with a 50× Zeiss objective (NA = 0.5, WD = 6.5 mm), after passing through an aperture with 500 μm diameter and a narrow-band-pass filter (546 nm ± 5 nm). The small aperture reduces the illumination angle for minimizing measurement errors. A normal electron multiplying charge-coupled device (EMCCD) camera (Andor) was used to acquire images. For the image analysis, MATLAB programs were used to analyze the interference images of nanowires to obtain both the inclined and azimuth angles. Sinusoidal fittings were used to obtain the periods of the interference patterns with subpixel resolution for calculating the inclined angles of the wires. On the other hand, a built-in function of MATLAB was used to fit the nanowire images with ellipsoids and calculate the azimuth orientations of their long axis.

To estimate the local rotational diffusivity of the nanowire, local rotational diffusivities in azimuth and inclination directions, respectively, were calculated from the linear slopes in Figs. 3(a) and 3(b) with the general law of random diffusion, $\langle \Delta\theta^2 \rangle = 2D_\theta \Delta t$. In Fig. 8, from bottom to top, blue plots are 0.01 rad at $t = 0$, green are 0.03, red are 0.09, and black are 0.19. Each color is corresponding to that plot in Figs. 3(a) and 3(b). At the short time scales below 0.05 s, the diffusivity value approximately remained constant, validating measurement of the local diffusivity. At long time scales, the nanowire moved to different positions, where they experienced different HI and the confinement effects from environments, resulting in deviation from the original local D_θ.

APPENDIX B: SIMULATION

For developing the implicit hydrodynamic beads–based model, as we concisely introduced in the main text, we first consider two representative beads B_i located at $\vec{X}_i$. If B_i moves with a steady speed $\vec{v}_i$ in the Stokes regime, its induced solvent flow at the location $\vec{X}_j$ can be determined as radial ($v_{r\_i,j}$) and

tangential ($v_{\theta\_i,j}$) as

$$v_{r\_i,j} = \left(\frac{3a}{2|\vec{r}_{ij}|} - \frac{a^3}{2|\vec{r}_{ij}|^3}\right)|\vec{v}_i|\cos\theta_{ij},$$
$$v_{\theta\_i,j} = -\left(\frac{3a}{4|\vec{r}_{ij}|} + \frac{a^3}{4|\vec{r}_{ij}|^3}\right)|\vec{v}_i|\sin\theta_{ij}, \tag{B1}$$

where we define $\vec{r}_{12} = \vec{X}_2 - \vec{X}_1 = \{x,y,z\}$ and angle θ_{ij} by $\cos\theta_{ij} = \frac{\vec{r}_{ij}\cdot\vec{v}_i}{|\vec{r}_{ij}||\vec{v}_i|}$.

Under this Stokes regime assumption, the general hydrodynamic relations between beads can be represented as

$$\vec{v}_{i,j} = T_{ij}\vec{v}_i, \tag{B2}$$

$$T_{12} = \left[C^{(1)}_{3\times1}, C^{(2)}_{3\times1}, C^{(3)}_{3\times1}\right], \tag{B3}$$

where

$$C^{(1)}_{3\times1} = \left(\frac{3a}{2|\vec{r}_{1,2}|^3} - \frac{a^3}{2|\vec{r}_{1,2}|^5}\right)\begin{Bmatrix}x^2\\xy\\xz\end{Bmatrix} - \left(\frac{3a}{4|\vec{r}_{1,2}|^3} - \frac{a^3}{4|\vec{r}_{1,2}|^5}\right)\sqrt{\frac{|\vec{r}_{1,2}|^2 - x^2}{y^2+z^2}}\begin{Bmatrix}-(y^2+z^2)\\xy\\xz\end{Bmatrix}, \tag{B4}$$

$$C^{(2)}_{3\times1} = \left(\frac{3a}{2|\vec{r}_{1,2}|^3} - \frac{a^3}{2|\vec{r}_{1,2}|^5}\right)\begin{Bmatrix}xy\\y^2\\yz\end{Bmatrix} - \left(\frac{3a}{4|\vec{r}_{1,2}|^3} - \frac{a^3}{4|\vec{r}_{1,2}|^5}\right)\sqrt{\frac{|\vec{r}_{1,2}|^2 - y^2}{x^2+z^2}}\begin{Bmatrix}xy\\-(x^2+z^2)\\yz\end{Bmatrix}, \tag{B5}$$

$$C^{(3)}_{3\times1} = \left(\frac{3a}{2|\vec{r}_{1,2}|^3} - \frac{a^3}{2|\vec{r}_{1,2}|^5}\right)\begin{Bmatrix}xz\\yz\\z^2\end{Bmatrix} - \left(\frac{3a}{4|\vec{r}_{1,2}|^3} - \frac{a^3}{4|\vec{r}_{1,2}|^5}\right)\sqrt{\frac{|\vec{r}_{1,2}|^2 - z^2}{x^2+yz^2}}\begin{Bmatrix}xy\\yz\\-(x^2+y^2)\end{Bmatrix}. \tag{B6}$$

By applying this representation to the generalized Eq. (3), which is developed in the main text and implicitly models the hydrodynamics of the system composed of N beads,

$$\vec{v}_{iH} + \sum_{j=1,j\neq i}^{N}\vec{v}_{jH,i} = \vec{v}_i, \tag{3}$$

we rewrite Eq. (3) as the following linear algebraic equation to implicitly solve the hydrodynamic problem.

$$\begin{bmatrix}I_{3\times3} & T_{21} & \cdots & T_{N1}\\ T_{12} & I_{3\times3} & \cdots & T_{N2}\\ \vdots & \vdots & \vdots & \vdots\\ T_{1N} & T_{2N} & \cdots & I_{3\times3}\end{bmatrix}_{3N\times3N}\begin{Bmatrix}\vec{v}_{1h}\\\vec{v}_{2h}\\\vdots\\\vec{v}_{Nh}\end{Bmatrix}_{3N\times1} = \begin{Bmatrix}\vec{v}_1\\\vec{v}_2\\\vdots\\\vec{v}_N\end{Bmatrix}_{3N\times1}. \tag{B7}$$

As shown in Fig. 9, simulation of the hydrodynamic effect between the nanowire and the wall was performed by incrementally increasing the extent of the wall matrix until computational results were asymptotically converged. The wire's configuration was fixed with the largest wire length and the highest inclined angle (24 μm = 160 beads as the wire length and 0.2 rad for the inclined angle), which requires the largest wall matrix. In other words, if the calculation converges with this wire's configuration, it should converge with all the other configurations (shorter wires and smaller inclined angles). n_x is the number of beads in the wall, extending perpendicular to the wire longitudinal direction (x axis), which is the width of the wall. n_{-y} is the number of beads in the wall, extending parallel into the wire's longitudinal direction (y axis) from the wire-wall contact. n_{+y} is the number of beads in the wall, extending parallel into the wire's longitudinal direction (y axis) from the point 160 beads (wire length) away from the contact. So, the height of the wall is the sum of n_{-y}, 160 beads (wire length), and n_{+y}. In calculation, n_{-y} and n_{+y} were set to be 20 and 90, respectively, with which the calculation results converged in increasing either n_{-y} or n_{+y} at any n_x. In increasing n_x, at last, the convergences of the calculated angular rotational diffusivities in both inclined and azimuth directions were confirmed as seen in the graph. The convergence in D_ϕ was much slower than that in D_θ and therefore requires a larger matrix. In Fig. 4(c), we used $n_x = 30$ for calculating the inclined angular diffusivity, D_θ, and using $n_x = 75$ for calculating the azimuth angular diffusivity, D_ϕ.

Using the developed implicit hydrodynamic bead model, we numerically calculated free rotational diffusivity of the nanowire and compared it with that of the analytical approximation as shown in Fig. 10. The analytical solution for a thin rod is given as the following equation and the result is plotted

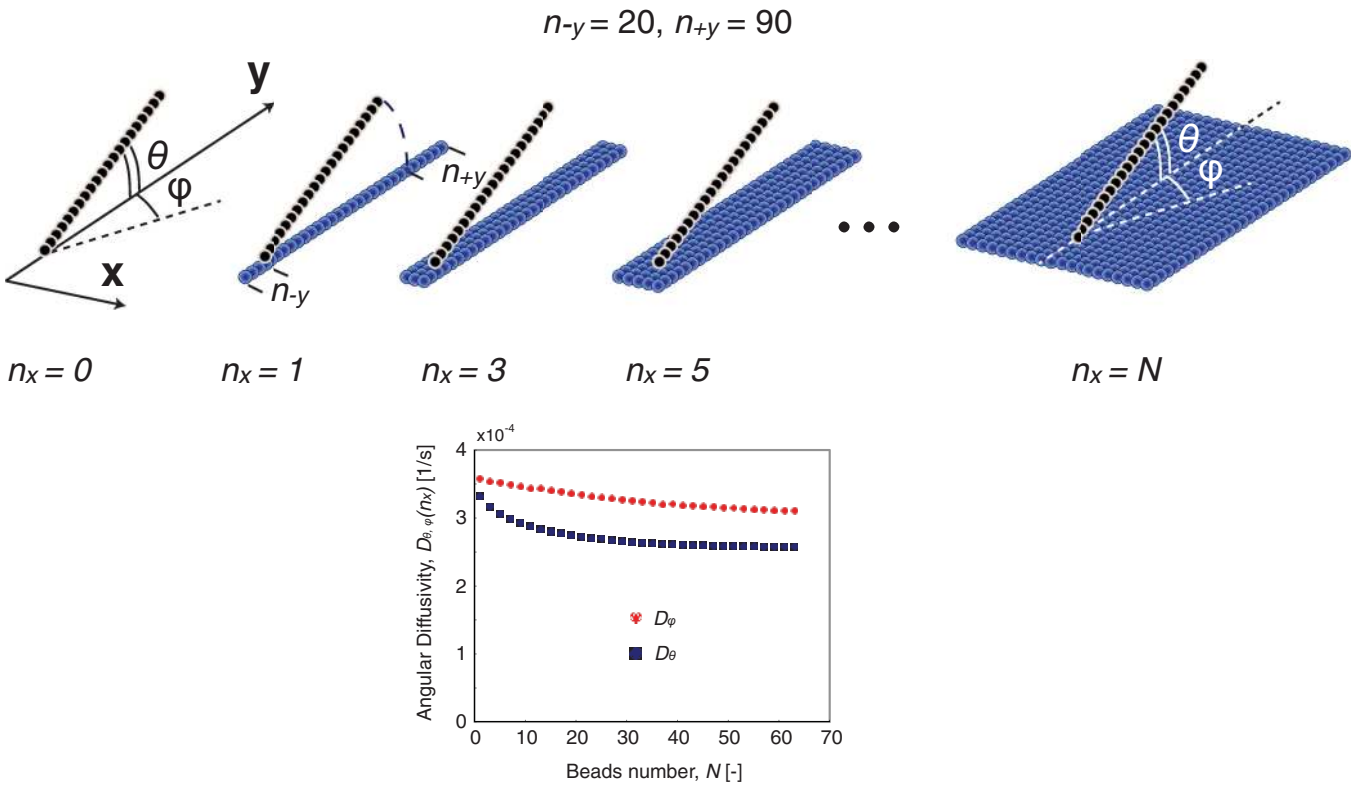

FIG. 9. (Color online) A schematic of simulation of the hydrodynamic effect between the nanowire and the wall. Its validness was confirmed by incrementally increasing the extent of the wall matrix until computational results were asymptotically converged.

as [14]:

$$D_{\text{rot}} = \frac{k_B T}{\zeta_{\text{rot}}} = k_B T/\pi\mu_w[L^3/\{3\ln(L/d) - 0.5\}]. \quad \text{(B8)}$$

The numerical result calculated by our hydrodynamics model is plotted as black circles and shows good agreement with the analytical curve, proving that our hydrodynamic model correctly considers complex intrinsic HI.

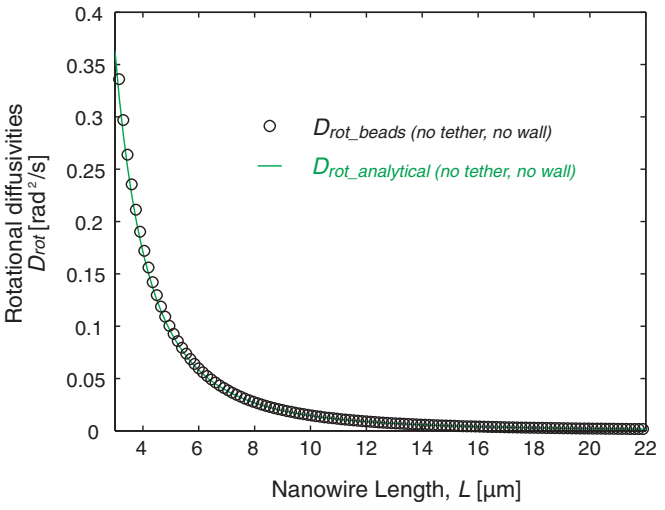

FIG. 10. (Color online) Comparison between the analytical approximation and the beads model for the rotational diffusion of the free nanowire *around its center*.

Next, we calculated rotational diffusivity of the nanowires between the inclined and azimuth angular rotational diffusion at a fixed angle for different lengths using the implicit hydrodynamic bead model (Fig. 11). The black circles are free rotational diffusivity of the tethered wire around its end, D_{rot}, numerically calculated using our developed bead model (without a wall). The filled (D_θ) and empty (D_φ) squares

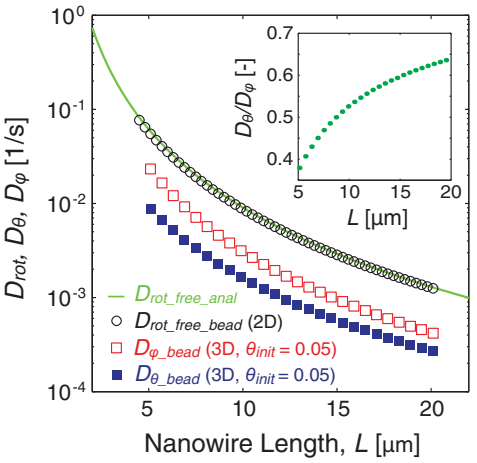

FIG. 11. (Color online) Comparison of rotational diffusivities of the nanowire between the inclined and azimuth angular rotational diffusion at a fixed angle for different length of wires, simulated by the implicit hydrodynamic bead model. In addition, those free nanowires estimated by analytical solution and calculated by the developed model were plotted together.

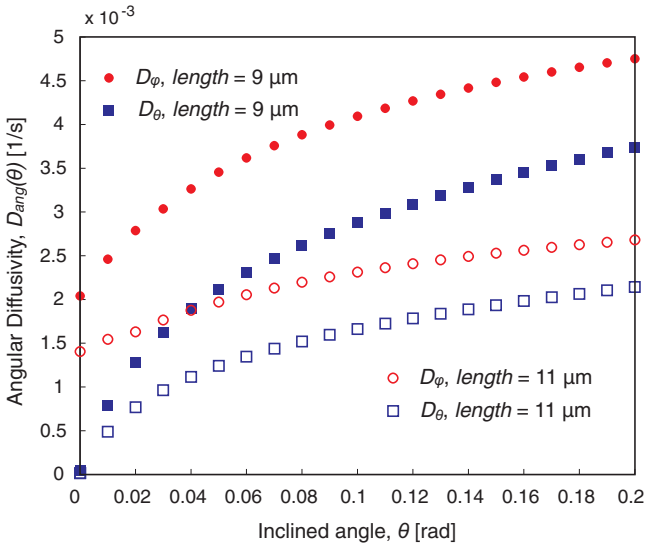

FIG. 12. (Color online) Comparison of rotational diffusivities of the nanowire between the inclined and azimuth angular rotational diffusion at different inclined angles for a fixed length of nanowires, simulated by the implicit hydrodynamic bead model.

are also the numerically calculated rotational diffusivities for the tethered wire in the inclined and azimuth directions, respectively (with a wall). The curve is the analytically approximated rotational diffusivity of the nanowire around its one end in bulk, $D_{\rm rot}$, for comparison [without a wall, see Eq. (B8)]. The inset plots the diffusional anisotropy (D_θ/D_φ). Here, the inclined angle is assumed 0.05 rad. The calculated D_θ and D_φ as well as the anisotropy in diffusivity showed good agreement with the experimental results shown in Fig. 2(b), validating our bead model for studying the hydrodynamic wall effect.

Finally, we calculated rotational diffusivity of the nanowires between the inclined and azimuth angular rotational diffusion at different inclined angles for a fixed length of nanowires using the implicit hydrodynamic bead model (Fig. 12). We calculated both inclined and azimuth rotational diffusivity of the samples' nanowires of 9 and 11 μm in length. The hydrodynamic drag by the wall appears as the reduction in the diffusivities when the nanowire becomes closer to the wall. As expected from the experiment, the effect was clearly less significant on D_φ, compared to that on D_θ, resulting in their highly anisotropic diffusion.

[1] K. Drescher, J. Dunkel, L. H. Cisneros, S. Ganguly, and R. E. Goldstein, Proc. Natl. Acad. Sci. USA **108**, 10940 (2011).
[2] I. H. Riedel, K. Kruse, and J. Howard, Science **309**, 300 (2005).
[3] E. Lauga, W. R. DiLuzio, G. M. Whitesides, and H. A. Stone, Biophys. J. **90**, 400 (2006).
[4] G. Li, L.-K. Tam, and J. X. Tang, Proc. Natl. Acad. Sci. USA **105**, 18355 (2008).
[5] C. Brennen and H. Winet, Annu. Rev. Fluid Mech. **9**, 339 (1977).
[6] I. S. Aranson and L. S. Tsimring, Phys. Rev. E **74**, 031915 (2006).
[7] N. Fakhri, F. C. MacKintosh, B. Lounis, L. Cognet, and M. Pasquali, Science **330**, 1804 (2010).
[8] G. Yu, A. Cao, and C. M. Lieber, Nat. Nanotechnol. **2**, 372 (2007).
[9] E. M. Freer, O. Grachev, X. Duan, S. Martin, and D. P. Stumbo, Nat. Nanotechnol. **5**, 525 (2010).
[10] Y. Huang, X. Duan, Q. Wei, and C. M. Lieber, Science **291**, 630 (2001).
[11] P. J. Pauzauskie, A. Radenovic, E. Trepagnier, H. Shroff, P. Yang, and J. Liphardt, Nat. Mater. **5**, 97 (2006).
[12] Y. Han, A. M. Alsayed, M. Nobili, J. Zhang, T. C. Lubensky, and A. G. Yodh, Science **314**, 626 (2006).
[13] J. T. Padding and W. J. Briels, J. Chem. Phys. **132**, 054511 (2010).
[14] A. Neild, J. T. Padding, L. Yu, B. Bhaduri, W. J. Briels, and T. W. Ng, Phys. Rev. E **82**, 041126 (2010).
[15] M. Trebbin, D. Steinhauser, J. Perlich, A. Buffet, S. V. Roth, W. Zimmermann, J. Thiele, and S. Forster, Proc. Natl. Acad. Sci. USA **110**, 6706 (2013).
[16] H. Brenner, Int. J. Multiphase Flow **1**, 195 (1974).
[17] G. Li and J. X. Tang, Phys. Rev. E **69**, 061921 (2004).
[18] T. L. Dodd, D. Hammer, A. S. Sangani, and D. L. Koch, J. Fluid Mech. **293**, 147 (1995).
[19] P. L. Chandran and M. R. K. Mofrad, Phys. Rev. E **81**, 031920 (2010).
[20] G. M. Wang, R. Prabhakar, and E. M. Sevick, Phys. Rev. Lett. **103**, 248303 (2009).
[21] M. D. Carbajal-Tinoco, R. Lopez-Fernandez, and J. L. Arauz-Lara, Phys. Rev. Lett. **99**, 138303 (2007).
[22] S. Jeney, B. Lukić, J. A. Kraus, T. Franosch, and L. Forró, Phys. Rev. Lett. **100**, 240604 (2008).
[23] H. Brenner, Chem. Eng. Sci. **16**, 242 (1961).
[24] G. Kasper, J. Aerosol Sci. **18**, 457 (1987).
[25] D. Li, N. Fakhri, M. Pasquali, and S. L. Biswal, Phys. Rev. Lett. **106**, 188302 (2011).
[26] See Supplemental Material at http://link.aps.org/supplemental/10.1103/PhysRevE.89.053010 for supplemental movies S1–S3.
[27] L. Limozin and K. Sengupta, ChemPhysChem **10**, 2752 (2009).
[28] H. C. Van De Hulst, in *Light Scattering by Small Particles* (John Wiley & Sons, Inc., New York, 1957).
[29] T. Li, S. Kheifets, D. Medellin, and M. G. Raizen, Science **328**, 1673 (2010).
[30] P. Bieling, I. A. Telley, J. Piehler, and T. Surrey, EMBO Rep. **9**, 1121 (2008).
[31] C. von Ballmoos, A. Wiedenmann, and P. Dimroth, Annu. Rev. Biochem. **78**, 649 (2009).
[32] C. Wilhelm, Phys. Rev. Lett. **101**, 028101 (2008).
[33] J. B. Rovner, C. P. Lapointe, D. H. Reich, and R. L. Leheny, Phys. Rev. Lett. **105**, 228301 (2010).
[34] S. Q. Choi, S. Steltenkamp, J. A. Zasadzinski, and T. M. Squires, Nat. Commun. **2**, 312 (2011).
[35] P. Dhar, Y. Cao, T. M. Fischer, and J. A. Zasadzinski, Phys. Rev. Lett. **104**, 016001 (2010).